Tensile Properties, Micro-computed Tomography Defect Analysis, and Milling Performance of As-Built and Heat-Treated CuCrZr Parts Fabricated by Laser Powder Bed Fusion

UDC:669.35:620.18
Original scientific paper https://doi.org/10.46793/aeletters.2026.11.3.5

Subba Reddy Mundla[1*], Arungalai Vendan Subbiah[2], C. P. Paul[3], Arun Kumar Shettigar[1], Sudhakar C. Jambagi[1]

[1]Department of Mechanical Engineering, National Institute of Technology Karnataka, Surathkal, India
[2]Department of Electronics and Communication Engineering, Dayananda Sagar University, Bangalore South, Karnataka, India
[3]Raja Ramana Centre for Advanced Technology, Indore, India

Abstract:
Copper–chromium–zirconium (CuCrZr) is an age-hardenable copper alloy valued for its rare mix of high strength and thermal conductivity, making it a logical choice for heat sinks, divertor parts, and rocket-engine liners. Laser powder bed fusion (LPBF) can fabricate such parts with internal cooling channels that are difficult to machine conventionally; however, this process makes the alloy a bit softer and may eventually lead to the formation of internal pores or voids. This study focuses on how LPBF CuCrZr behaves, both mechanically and during milling, in the As-Built (AB) and heat-treated states. Vickers hardness rose from about 118 HV in the AB state to 152 HV after heat treatment. Tensile testing demonstrated the ultimate tensile strength improving from roughly 680–700 MPa to 780–820 MPa, a gain of about 15–18%, while total elongation remained at or above 95% for all heat-treated specimens. Micro-computed tomography (µCT) confirmed a dense build in both states, with relative density near 99% and no lack-of-fusion defects or cracking; only a few small, isolated gas pores were seen. In milling, the harder, heat-treated material required slightly higher cutting forces (CF) but produced a more stable cut and better surface finish, with the lowest 3D roughness at high cutting speed (CS) and low feed. Scanning Electron Microscopy (SEM), Energy-Dispersive Spectroscopy (EDS), and Atomic Force Microscopy (AFM) were used to characterize the microstructural, compositional, and surface-topographical changes, respectively, observed after heat treatment. Consequently, the heat treatment strengthens LPBF CuCrZr and improves surface finish without compromising the soundness or ductility.

ARTICLE HISTORY
Received: 21 July 2026
Revised: 10 September 2026
Accepted: 17 September 2026
Published: 23 September 2026

KEYWORDS
CuCrZr, Laser powder bed fusion, Heat treatment, Milling, Surface roughness, Cutting forces, Tensile behaviour, Micro-computed tomography

1. INTRODUCTION

CuCrZr alloys are widely used in the automotive, aerospace, nuclear and electrical sectors because they carry heat and current well while retaining strength, wear resistance and thermal stability. The growing use of LPBF in Additive Manufacturing (AM) has made it possible to build CuCrZr parts with shapes that are difficult or impossible to produce by conventional routes. Yet, parts leaving the LPBF machine usually need finishing steps such as machining and heat treatment before they reach the required surface quality, dimensional accuracy and mechanical

*CONTACT: Arungalai Vendan Subbiah, e-mail: arungalai-ece@dsu.edu.in

performance. Machining parts in their AB versus heat-treated state illustrates a noticeable difference. It alters the tool settings, maintains the production run repeatability, and ensures the final part holds up under stress. The key research articles contributing to this study are summarized in the following sections.

Heat treatment significantly modifies the microstructure and properties of LPBF-manufactured CuCrZr, and it further affects the machining of the alloy. In the case of an AB CuCrZr sample, it typically has a supersaturated copper matrix, illustrating coarse chromium precipitates jointly with residual stresses left by rapid solidification [1-3]. Solution annealing followed by age hardening (SAAH) enables precipitation that evenly spreads fine chromium-rich particles, which enhances the tensile strength, hardness, electrical conductivity and thermal stability [4]. Reports emphasize that the SAAH condition reaches higher strength, hardness and conductivity compared to the AB state [4, 5]. However, defects related to the process, such as. microcracks, gas pores and lack-of-fusion pores, are not fully eliminated by heat treatment and continue to influence fatigue life, which is higher than that of the static tensile behaviour [5]. Scan strategy, Scan path length, and part geometry also alter the formation of defects, the rate of melt cooling, and grain growth, and hence, they shape the final properties [6]. These investigations agree with wider studies on AM metals, which connect processing conditions to microstructure and subsequently, to mechanical response [7].

Recent research confirms that AM is an efficient way to fabricate high-density CuCrZr with improved performance compared with conventional techniques. Relative densities as high as 99.7% and 99.8% have been attained with the deployment of LPBF and Electron-Beam Powder Bed Fusion (EB-PBF), respectively [8, 9]. Green laser systems operating at 532 nm improve laser absorption in copper alloys and can achieve relative densities approaching 99.6%, thereby reducing the occurrence of defects commonly associated with infrared laser processing [10]. These refined approaches give fine microstructures and precipitates, respectively, which increase hardness and strength. Appropriate control of ageing time and temperature is essential to get the most out of precipitation strengthening without losing conductivity [3]. Combining AM with alloy-design choices also lets CuCrZr be tuned for a given application by using the shape freedom of LPBF [10]. Broader reviews add that laser wavelength, volumetric energy density, powder quality and scan strategy all affect densification, microstructural refinement and final performance [7, 11].

Several groups have studied how different finishing routes change CuCrZr made by various AM methods. In electro-discharge machining, thermo-mechanical processing (hydrostatic extrusion followed by ageing) has been shown to cut electrode wear sharply while raising hardness [12]. Alongside heat treatment, process optimisation during LPBF is a key control on precipitation, residual stress and defect formation [11]. For Wire-Arc Additive Manufactured (WAAM) CuCrZr, SAAH gives the best mix of conductivity and strength through fine, evenly spread chromium precipitates [4]. For LPBF CuCrZr, direct ageing near 450 °C has been reported to form nanoscale chromium precipitates that raise both strength and conductivity [13]. In short, the appropriate thermal schedule depends on the AM method used.

Process-parameter tuning yields further gains. Work on Selective Laser Melting (SLM) shows that raising laser power while lowering scan speed improves part density and mechanical properties, and that hatch spacing controls defect formation and melt-pool stability, with an optimum band beyond which performance drops [14]. Volumetric energy density has likewise been reported as a key control on grain refinement, porosity and precipitation in LPBF CuCrZr, which then feeds directly into how the material machines.

While much has been done on the mechanical properties and microstructure of LPBF CuCrZr, far less has looked at how the material machines after AM. Heat treatment changes ductility, hardness, precipitate shape and residual-stress distribution, and all of these affect chip formation, CF, surface quality and tool wear during milling. Careful characterisation using SEM with EDS and AFM gives useful insight into subsurface damage, topography and wear. This study helps select the right finishing route and maintain the accuracy and functionality of critical parts.

End milling is the most common machining operation for LPBF copper alloys. Feed Rate (FR), CS, and Depth of Cut (DoC) determine surface quality, which drives chip removal, cutting temperature, material-removal behaviour, and tool wear [15, 16]. In general, higher CS improves finish by limiting built-up edge and providing a steadier cut, whereas higher feed usually increases roughness and CF. Balancing productivity against

surface integrity therefore requires careful selection of machining settings [17]. Tool wear and surface roughness (Sa) are the two most-used measures of machinability because they bear directly on part performance, cost, accuracy and tool life.

A thorough literature review shows that, although AM, heat treatment, and mechanical testing of CuCrZr are well covered, few studies have systematically examined milling of LPBF CuCrZr, and even fewer have directly compared the AB and heat-treated states. Almost none have used a statistically designed experiment to tune the machining settings while, at the same time, tying the results to surface integrity, tool wear, CF, hardness and microstructure. The present study addresses that gap. It is, to the authors' knowledge, the first to combine, on the same LPBF CuCrZr material and in both conditions: (i) a five-level central composite rotatable design (CCRD) for the milling trials; (ii) measured hardness before and after heat treatment; (iii) tensile behaviour of four specimens per condition; and (iv) µCT of the internal pore population. Bringing machinability, bulk mechanical response and internal soundness together on one material is what sets this work apart from earlier single-topic studies [3, 4, 13]. This research aims to provide practical guidance for selecting an appropriate finishing route and machining window for LPBF CuCrZr parts intended for demanding service conditions.

2. MATERIALS AND METHODS

This study compares LPBF CuCrZr in the AB and heat-treated conditions across three fronts: hardness and tensile behaviour, internal soundness, and milling performance. The alloy was built by LPBF on an STLR 400 machine (Fig. 1, Amace Solutions, Bengaluru, India). Test samples were cut from the builds by wire electrical discharge machining (WEDM). Heat treatment was carried out in a furnace under an argon cover. Vickers hardness was measured on a micro-hardness tester following ASTM E384. Milling trials were run on a 3-axis CNC vertical machining centre using a Kistler piezoelectric dynamometer to record CF in three directions. Three-dimensional Sa was measured with a 3D optical profilometer according to ISO 25178. Tensile tests followed ASTM E8/E8M on a servo-hydraulic universal testing machine. Internal defects were examined by µCT. Microstructure and topography were studied by SEM, EDS and AFM. The milling experiment was laid out as a five-level CCRD, and the data were analysed with Design-Expert and Python (pandas, NumPy, scikit-learn, Matplotlib) for regression and partial-correlation analysis.

Fig 1. LPBF machine (STLR 400) used to build the CuCrZr parts [18]

2.1 LPBF Build of CuCrZr

CuCrZr powder with a particle size range of 15–45 µm was used, chosen for good flow and packing during spreading. The LPBF machine melts and fuses the powder layer by layer with a focused laser that follows a set scan pattern to build the part [18]. The build settings were kept the same as in the authors' earlier study [18] on the same material to keep the two works comparable: laser power 340 W, scan speed 900 mm/s, hatch spacing 90 µm, and layer thickness 30 µm, under an argon atmosphere. The first build was a 110 mm × 110 mm × 8 mm plate. LPBF can make complex shapes, but a plate was used here because it suits milling trials; it was later cut into smaller samples by WEDM at the Advanced Manufacturing Lab, NITK Surathkal.

2.2 Heat Treatment

Heat treatment of AB CuCrZr is needed to restore the electrical and mechanical properties that rapid solidification leaves incomplete, because the AB structure holds non-equilibrium phases, high residual stress and little precipitation hardening. A two-stage schedule was adopted. First, solution annealing was carried out at 980 ± 5 °C for 1 h to dissolve chromium and zirconium into the copper matrix; then, water quenching was performed to retain them in solid solution. This was followed by ageing treatment at 460 ± 5 °C for 3 h to precipitate the fine Cr-rich and Cu–Zr particles, which were then cooled. A muffle furnace was deployed in both stages under a flowing-argon cover to restrict oxidation, with a

heating rate of about 10 °C/min. This heat-treatment schedule was selected based on previously reported solution-treatment and ageing conditions for LPBF CuCrZr [13].

The impact of this treatment on hardness was directly measured. Vickers hardness (HV0.5, 10 s dwell, ASTM E384) was measured as the mean of ten indents per condition. Hardness increased from 118 ± 6 HV in the AB state to 152 ± 7 HV post heat treatment, an increase of approximately 29%. This observation clearly shows that heat treatment hardens the alloy through precipitation. This confirms that heat treatment raises hardness relative to the AB state and that the harder material tends to load the tool slightly more. However, the treatment does not soften the alloy below the AB level. The process of "softening" was, in fact, the relief of residual stress and the removal of the local brittle, hard, non-uniform regions of the AB structure. This change enables steady cutting and a smoother surface, even though the average hardness is higher. The milling results in Section 3 are interpreted along these lines.

2.3 Wire-Cut EDM

WEDM removes material with an electrically charged brass wire while the part sits in a dielectric fluid (deionised water) that cools the region and flushes away debris. It gives fine, complex cuts with high precision and little thermal distortion [19, 20]. After building, the 110 mm × 110 mm × 8 mm plates were cut into smaller samples by WEDM to 110 mm × 50 mm × 8 mm. Fig. 2 shows the AB specimen used for milling, including the trial markings and parameter range.

The high thermal conductivity of CuCrZr can set up thermal stresses during LPBF; these were controlled through the build settings presented above. LPBF parts need finishing by WEDM or machining to reach final size and finish, which adds time and cost. CuCrZr powder was cautiously handled to avoid contamination and to maintain consistent quality.

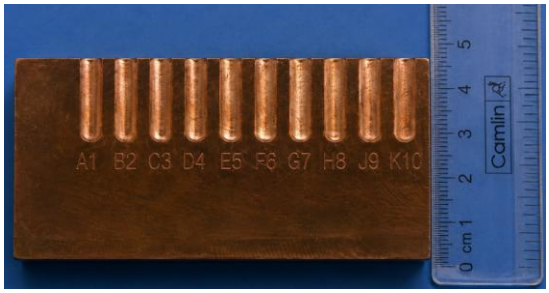

Fig 2. AB CuCrZr specimen used for milling

2.4 Milling Trials

The milling trials, conducted using customized machining settings—namely CS, FR, and DoC—investigated their effects on the CF and machined surface. The objective was to determine the settings that provided an accurate and durable surface on CuCrZr parts intended for demanding service conditions. Milling was performed on a 3-axis CNC vertical machining centre.

Table 1 specifies the cutting tool details, which will help correlate the wear discussion conclusions that may be drawn from it.

Table 1. End-mill specification used in the milling trials

TOOL FEATURE	SPECIFICATION
Tool type	Solid end mill (flat)
Tool material	Cemented tungsten carbide (WC–Co)
Coating	Titanium aluminium nitride (TiAlN)
Diameter	8 mm
Number of flutes (teeth)	4
Helix angle	30°
Nose/corner radius	0.5 mm
Overhang length	25 mm
Coolant	Dry cutting

The experimentation and testing adhered to recognised standards. Tensile testing was performed as per ASTM E8/E8M standards, while hardness was measured as per ASTM E384. The 3D roughness measurements followed ISO 25178. CF was recorded with a Kistler three-component piezoelectric dynamometer mounted under the workpiece; the charge signals were passed through a charge amplifier and logged, giving the force components *Fx, Fy* and *Fz.* Sa is the arithmetic mean of the absolute surface height over the measured area, i.e., the 3D counterpart of the familiar 2D Ra. It was measured using a 3D optical profilometer according to ISO 25178 over a 1 mm × 1 mm area, with a Gaussian filter used to separate roughness from form. Each surface was measured at three separate spots, and the mean was reported. Every milling condition was repeated three times; the values in Tables 3 and 4 are the means, and the run-to-run scatter was within ±6% for Sa and ±8% for the resultant CF. This scatter is the experimental error carried through the analysis.

The FR values of 65–235 mm/min are table-feed values for an 8 mm carbide end mill in copper (Tables 3 and 4). The regression coefficients were computed per unit.

The milling settings were based on a three-factor, five-level CCRD, comprising 20 experimental runs as shown in Table 2. CCRD was selected because it enables the detection of curvature in the response while requiring a manageable number of experimental runs. The rotatable form provides an even prediction quality in all directions from the centre. The design presents 20 runs: 8 factorial points, 6 axial points at the rotatable distance of α = 1.682, and 6 centre points that provide a direct read on repeatability. Here, α (alpha) is the axial distance from the centre point (0) beyond the coded range −1 to +1 in a Central Composite Rotatable Design (CCRD).

Table 2. CCRD factors and their five levels used during the milling operations

Factor	Unit	−α (Lower axial point)	Low (−1)	Centre (0)	High (+1)	+α Upper axial point)
CS	rpm	490	1000	1750	2500	3010
FR	mm/min	65	100	150	200	235
DoC	mm	0.30	0.40	0.55	0.70	0.80

2.5 Milling of Heat-Treated CuCrZr

Milling heat-treated material is more challenging because the alloy hardens after ageing and work-hardens. The increase in hardness can reduce the tool life, leading to the adoption of coated carbide tools and an appropriate high CS to maintain a clean and accurate surface [18]. Good chip clearance is important for ensuring tool cooling and elimination or minimization of the surface defects. With these settings, the heat-treated material maintained its size while retaining the strength gained from ageing. Fig. 3 shows the heat-treated specimen after milling, including its trial markings and parameter range.

Fig. 3. Heat-treated CuCrZr showing the milled section

Table 3 lists the 20 CCRD runs for the AB material with the measured 3D Sa and the three cutting-force components. All the results in Table 3 belong to the AB samples.

Table 4 reproduces the 20 CCRD milling trials for the heat-treated CuCrZr condition reported in the authors' previous study [18]. These data are included here to enable direct comparison with the AB condition. One trial (Std. 11) records an unusually high CF and is therefore treated as an incorrect measurement in the analysis, as noted in Section 3.

Table 3. CCRD milling trials for *AB* CuCrZr

Std	Run	CS (rpm)	FR (mm/min)	DoC (mm)	Sa (nm)	Components of the CF		
						Fx (N)	Fy (N)	Fz (N)
8	1	2500	200	0.7	0.78	-2.03	-19.43	-3.34
2	2	2500	100	0.4	0.73	-0.15	-14.57	-3.67
17	3	1750	150	0.55	6.97	-0.64	-27.15	-3.75
19	4	1750	150	0.55	5.96	-0.42	-15.36	-3.69
14	5	1750	150	0.8	6.38	-5.26	-54.60	-16.06
20	6	1750	150	0.55	6.30	-2.64	-24.44	-10.51
15	7	1750	150	0.55	6.67	-3.19	-26.54	-7.51
6	8	2500	100	0.7	0.54	-5.81	-30.98	-11.08
18	9	1750	150	0.55	6.99	-4.86	-58.44	-10.21
12	10	1750	235	0.55	5.72	-2.11	-21.91	-5.87
13	11	1750	150	0.3	6.50	-0.49	-12.52	-1.69
7	12	1000	200	0.7	2.16	-0.45	-19.39	-2.76
1	13	1000	100	0.4	1.74	-6.80	-10.24	-0.16
9	14	490	150	0.55	2.93	-9.67	-41.45	-10.55
4	15	2500	200	0.4	1.15	-5.21	-20.42	-4.32
10	16	3010	150	0.55	0.57	-7.15	-18.46	-3.54
3	17	1000	200	0.4	2.32	-13.85	-22.19	-4.55
11	18	1750	65	0.55	6.05	-11.89	-16.95	-2.06
5	19	1000	100	0.7	1.61	-14.60	-11.52	0.53
16	20	1750	150	0.55	6.64	-17.18	-15.67	-0.39

Table 4. CCRD milling trials for heat-treated CuCrZr, reproduced from [18]

Std	Run	CS (rpm)	FR (mm/min)	DoC (mm)	Sa (nm)	Components of the CF		
						Fx (N)	Fy (N)	Fz (N)
8	1	2500	200	0.7	0.92	45.01	3.36	-4.88
2	2	2500	100	0.4	0.48	-0.907	-7.78	-0.27
17	3	1750	150	0.55	12.68	-0.38	-14.16	-1.45
19	4	1750	150	0.55	11.30	-0.49	-8.41	-0.53
14	5	1750	150	0.8	11.82	-8.40	-36.09	-5.08
20	6	1750	150	0.55	12.31	-5.03	-16.65	-1.86
15	7	1750	150	0.55	10.80	-5.30	-29.11	-5.04
6	8	2500	100	0.7	0.44	-5.39	-20.89	-3.38
18	9	1750	150	0.55	8.83	-2.40	-34.66	-4.36
12	10	1750	235	0.55	9.29	-1.83	-9.21	-1.33
13	11	1750	150	0.3	10.62	-47.03	-81.08	-60.56
7	12	1000	200	0.7	2.16	-2.67	-10.95	-0.01
1	13	1000	100	0.4	0.65	-0.37	-8.26	4.60
9	14	490	150	0.55	2.48	-13.49	-36.69	-7.91
4	15	2500	200	0.4	0.65	-9.23	-23.56	-7.62
10	16	3010	150	0.55	0.70	-8.14	-20.87	-5.53
3	17	1000	200	0.4	1.95	-5.91	-15.42	-4.57
11	18	1750	65	0.55	5.34	-9.25	-22.25	-5.56
5	19	1000	100	0.7	1.24	-9.34	-16.79	-6.79
16	20	1750	150	0.55	12.37	-8.94	-21.50	-5.86

2.6 Analysing Tensile Behaviour and Internal Defects

Tensile behaviour and internal soundness of LPBF CuCrZr were analysed for both untreated and heat-treated cases. The tensile specimens were prepared from a separate cylindrical LPBF build, 30 mm in diameter, distinct from the 110 mm × 110 mm × 8 mm plate used for the milling trials. A total of eight tensile specimens were prepared. From the cylindrical build, 70 mm blanks were cut by WEDM into cylindrical pieces roughly 10 mm in diameter and machined to the ASTM E8/E8M tensile geometry. Four specimens (A1–D4) were retained in the AB condition, while four specimens (E5–H8) were subjected to the solution annealing and ageing treatment before final machining. Each specimen was threaded at both ends to form the gauge length, and progressively lighter finishing passes were used on the gauge section to keep the machining-affected layer shallow. All eight specimens were tested to failure in uniaxial tension, with the engineering stress–strain curve recorded for each. The same specimens were subsequently scanned by μCT to examine the internal pores. Pore equivalent diameter, defined as the diameter of a sphere having the same volume as the pore, was used as the pore-size measure.

3. RESULTS AND DISCUSSION

The research results are presented in two parts. The first uses a Partial Correlation Heat Map (PCHM) and regression to read the milling data. The second covers hardness testing and characterisation of the specimens by SEM, EDS and AFM. The third covers tensile behaviour of four specimens per condition and μCT of the internal pore population.

3.1 PCHM Analysis

3.1.1 PCHM: AB CuCrZr

A PCHM shows the direct connection between two variables once the effect of the others is removed, which makes it a cleaner tool than a plain correlation matrix for reading interacting machining parameters [21].

For the AB data (Table 3), the strongest positive link is between *Fy* and *Fz* (r = 0.83), meaning the transverse and thrust force components rise and fall together. CS shows a moderate positive link with *Fx* (r = 0.31), and FR a similar one (r = 0.28), so both settings push the force along X.

The output measures connect only weakly to the process parameter settings. DoC shows weak negative correlation with *Fx* (r = −0.10), *Fy* (r = −0.12) and *Fz* (r = −0.14), so no single force component controls how deep the cut runs once the rest is held fixed. Sa likewise links weakly, most

strongly (and negatively), with *Fy* (r = −0.26) and with CS (r = −0.21). The picture is one of tightly coupled force components but only a limited direct pull from any one setting on the output (Fig. 4).

A multiple linear regression was fitted with CS (rpm), FR (mm/min), and DoC (mm) as the independent variables and Sa (nm) as the response. The resultant CF was analysed separately as a measured response using the same three machining inputs. Here, CF denotes the resultant CF calculated from the measured components as $CF = \sqrt{(Fx^2 + Fy^2 + Fz^2)}$.

$$Sa = 5.4217 - (8.3986\times10^{-4}\cdot CS) + (1.7837\times10^{-3}\cdot FR) - (0.5164\cdot DoC) \quad (1)$$

For the AB condition, the linear model gives R^2 = 0.043 for Sa, indicating a weak linear fit. A separate model for CF gives R^2 = 0.201, with DoC showing the largest positive coefficient. These models are descriptive within the investigated parameter range rather than predictive laws.

The corresponding regression for the resultant CF is given in Eq. (2):

$$CF = 3.9674 - (2.6536\times10^{-3}\cdot CS) + (1.6681\times10^{-2}\cdot FR) + (44.3761\cdot DoC) \quad (2)$$

For CF in the AB condition, DoC has the largest positive coefficient, while CS and FR have smaller effects. The relatively low R^2 (0.201) indicates that the linear model captures only part of the variation in the measured CF.

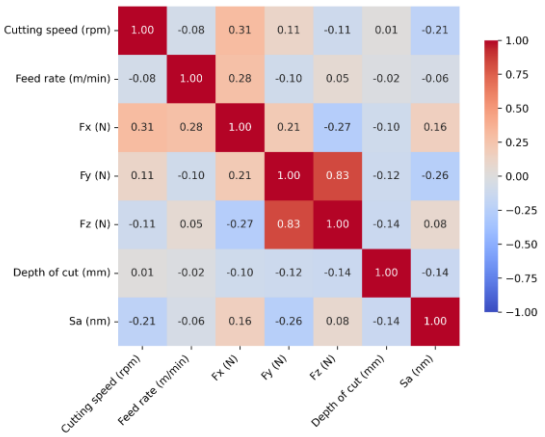

Fig. 4. PCHM for AB CuCrZr

3.1.2 PCHM: Heat-Treated CuCrZr

For the heat-treated CuCrZr samples, as presented in Table 4, the PCHM shows *Fy* and *Fz* strongly coupled (r = 0.77). Unlike the AB case, *Fx* correlates strongly with DoC (r = 0.42), and *Fz* moderately so (*r* = 0.32). In the heat-treated material, the force components feed more directly into how deep the cut runs. Among the settings, feed demonstrates a weak positive correlation with *Sa* (r = 0.20) and *Fy* a weak negative one (*r* = −0.22), while the direct linear association between CS and the measured responses is weak. Compared with the AB material, the heat-treated set reveals that the force components carry more of the response, especially DoC (Fig. 5).

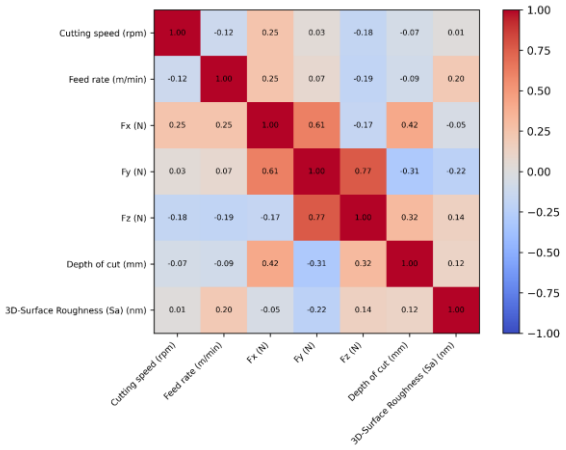

Fig. 5. PCHM for heat-treated CuCrZr

Roughness declines as CS increases because a faster spindle provides a finer, continuous cut. The thermal conductivity of copper being higher carries heat away from the edge, which restricts tool wear and facilitates holding the finish at speed. For the heat-treated condition, CS, FR, and DoC were used as independent variables in the regression models for Sa and CF. The single high-force run (Std. 11) was excluded from these regression calculations, consistent with the treatment described for the heat-treated dataset.

$$Sa = 0.6012 - (6.3520\times10^{-4}\cdot CS) + (1.3911\times10^{-2}\cdot FR) + (7.1459\cdot DoC) \quad (3)$$

For the heat-treated condition, the Sa model gives R^2 = 0.047, indicating a weak linear fit. The corresponding CF model gives R^2 = 0.178. These low R^2 values indicate that the simple linear models describe only part of the variation in the measured responses.

$$CF = -5.8192 + (1.4671\times10^{-3}\cdot CS) + (2.1478\times10^{-2}\cdot FR) + (39.6356\cdot DoC) \quad (4)$$

For the heat-treated condition, DoC, CS, and FR are the controlled machining inputs, while Sa and CF are the measured responses. The separate CF model shows a positive dependence on DoC within the investigated range, but the low R^2 indicates limited predictive capability.

The overall observations from this study agree with existing research reports for copper and copper-alloy milling. The observed trends of higher CS and lower feed producing a better surface finish are consistent with earlier machining-parameter reports [15, 16] and with WEDM work on copper that emphasizes higher speed to attain lower roughness [19]. The heat-treated material needs a higher, but steadier, force; this also maps to the general finding that a harder and more uniform microstructure cuts more predictably, even if it loads the tool slightly more. The measured relative density was observed to be above 99% and approximately the same as the 99.6–99.8% values reported for LPBF and EB-PBF CuCrZr [8-10], confirming that the build here is of comparable quality.

3.2 Testing and Characterisation

Vickers hardness was measured before and after heat treatment as described in Section 2.2; the mean rose from 118 ± 6 HV (AB) to 152 ± 7 HV (heat-treated). SEM examined surface morphology and microstructure, revealing grain boundaries, pores and precipitates. EDS gave the elemental distribution, in particular chromium (Cr) and zirconium (Zr) segregation or precipitation. AFM gave the nanoscale topography, which shows how heat treatment changes *Sa* [22]. All microscopy was done on the same specimens used for milling. SEM and EDS were carried out on a Carl Zeiss Field-Emission Scanning Electron Microscope (FESEM) fitted with an energy-dispersive X-ray detector, operated at 20 kV with a working distance of about 14.5 mm. AFM was carried out in tapping mode over a 10 µm × 10 µm area. Together, these methods provide important information on surface character and microstructural change.

3.2.1 SEM

Figs. 6a and 6b show SEM micrographs for the two conditions. In the AB state, large columnar grains run 100–500 µm long. This coarse columnar form results from the steep thermal gradient, which drives grains to grow along the build direction and suppresses new nucleation. The absence of dendrites or strong orientation patterns suggests the section underwent annealing-like thermal cycles during deposition. Porosity is low, pointing to a well-defined LPBF process with steady and uniform powder flow and laser control. Secondary-phase segregation is not visible in the AB micrograph. The high cooling rate of LPBF facilitates an even particle distribution.

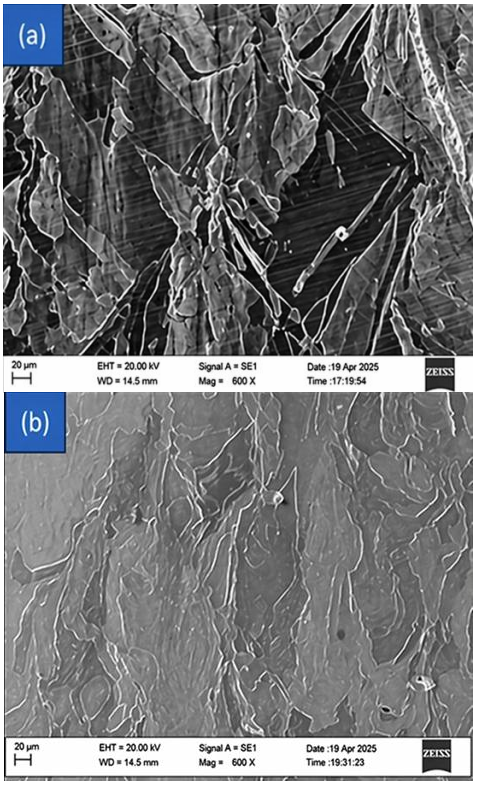

Fig. 6. SEM micrographs of LPBF CuCrZr in the transverse section: (a) AB and (b) heat-treated

After the heat treatment (Fig. 6b), the structure is more balanced. Grain boundaries are seen clearly, indicating that recrystallisation and stress relief occurred during the thermal exposure [22, 23]. The precipitates coarsen and adopt a more regular shape, as in the pattern of Ostwald ripening, with wider spacing between them. This gives a more stable phase distribution that facilitates ductility, thermal conductivity and long-term dimensional stability. In cases where the AB surface was rougher, associated with microcracks and partly sintered powder, the heat-treated surface is smoother, with little or no microcracks and an enhanced grain structure. The heat treatment evens out the microstructure and reduces internal stress, leading to the attainment of an improved milled surface.

This correlation justifies the milling data. The AB CuCrZr sample, with its harder, less uniform local structure, tends to accelerate cutting-edge wear and results in less stable cutting. The heat-treated sample, though harder on average, cuts steadily because the structure is uniform and the residual stress has been largely relieved, which eventually leads to the attainment of a smooth surface.

3.2.2 EDS

The EDS map of the AB material is shown in Fig. 7. An even spread of the main elements is observed, which emphasizes that copper acts as the matrix, with chromium and zirconium held in solid solution or as fine precipitates. In the AB state, Cr and Zr remain mostly in a supersaturated solid solution, with slight segregation because solidification is swift. EDS also records any surface oxidation or slight grain-boundary segregation. This proves that the starting composition is uniform before heat treatment.

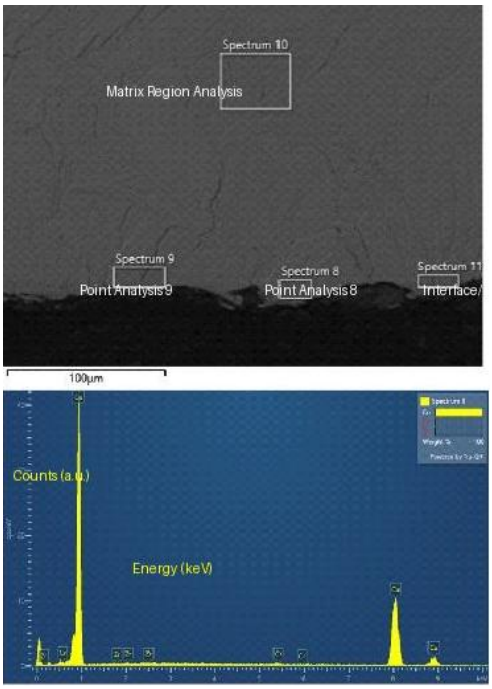

Fig. 7. SEM and EDS images of AB LPBF CuCrZr along the transverse section

Analysing the two conditions together from Figs. 7 and 8; it is clear that grain size and precipitate distribution govern the material cuts. In the AB sample, finer grains and uneven precipitates increase local hardness and CF, which wears the tool faster. After the heat treatment process, the precipitates coarsen, and the structure evens out, which reduces the local cutting resistance and gives a cleaner cut. These microstructural shifts directly affect chip formation, surface finish, and tool life.

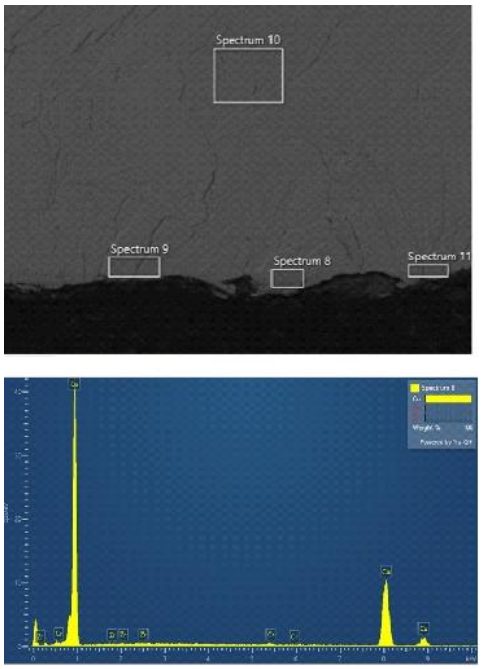

Fig. 8. SEM and EDS images of heat-treated LPBF CuCrZr in the transverse section

3.2.3 AFM Analysis

Fig. 9 shows the AFM scan of the AB surface. High roughness may be observed, which is due to the partly melted powder and the layer-by-layer build. Unmelted particles, sharp ridges along melt-pool boundaries, and fine undulations are all visible. These are typical features of an LPBF surface and can impact fatigue and conductivity, which emphasizes that AFM is useful for judging whether finishing steps are essential.

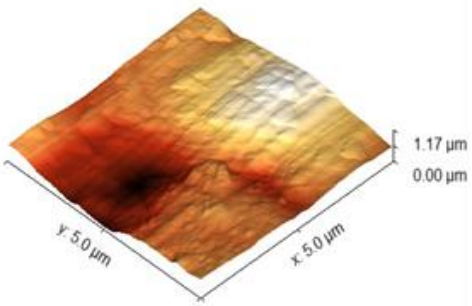

Fig. 9. AFM image of AB CuCrZr

After heat treatment, the surface is smoother, as shown in Fig. 10. Surface diffusion and stress relief during the thermal cycle round off fine asperities and reduce nanoscale roughness, consistent with the lower Sa measured on the milled surfaces. A few larger unmelted particle marks may remain, but the surface is more uniform, which indicates a more stable material and better performance where good electrical or thermal contact is needed.

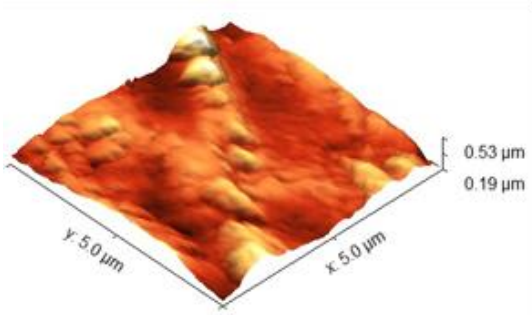

Fig. 10. AFM image of heat-treated CuCrZr

3.3 Tensile Behaviour and Internal Defects

3.3.1 Tensile Specimen Preparation

Tested specimens for both untreated and heat-treated conditions are shown in Fig. 11.

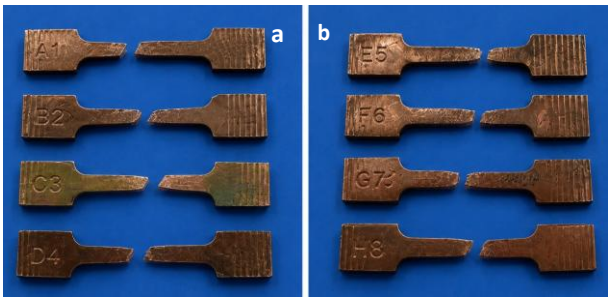

Fig. 11. CuCrZr tensile specimens: (a) AB and (b) heat-treated

3.3.2 Tensile Testing and µCT

Four specimens from each condition were pulled to failure in uniaxial tension to ASTM E8/E8M, and the engineering stress–strain curve was recorded for each. The same specimens were then scanned by µCT to examine the internal pores. Pore equivalent diameter, the diameter of a sphere with the same volume as the pore, was used throughout as the size measure, since it is the standard way to compare 3D pore populations from µCT.

3.3.3 AB CuCrZr

The AB specimens gave the classic ductile response: an elastic region, yield at low strain, a long strain-hardening stage, a broad Ultimate Tensile Strength (UTS) plateau, necking and fracture. A1 yielded at 140–160 MPa and hardened to a UTS of 685 MPa near 70–75% strain before fracturing at about 103% strain. B2 behaved similarly, reaching 690 MPa and fracturing near 100% strain. C3 gave the highest AB strength (700 MPa) at 70–75% strain, with total elongation of 101–102%, suggesting an especially uniform, low-defect blank. D4 fractured at a slightly lower stress after necking (680 MPa, 99–100% total elongation), most likely from local variation in porosity, residual stress or microstructure rather than any systematic effect.

The narrow UTS spread (680-700 MPa) indicates repeatable builds and a uniform structure from blank to blank. All four curves show a long strain-hardening region that delays necking, which fits the fine cellular-dendritic structure typical of rapid LPBF solidification and its ability to store dislocations. Table 5 lists the AB tensile properties, and Fig. 12 (a)-(d) correspond to specimens A1, B2, C3 and D4, respectively.

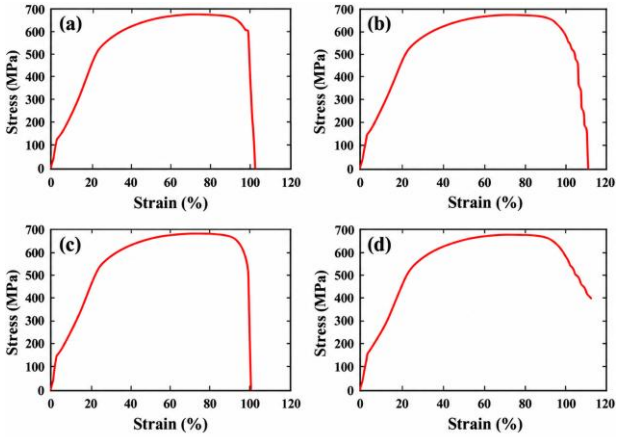

Fig. 12. Stress–strain curves of AB CuCrZr specimens: (a) A1, (b) B2, (c) C3 and (d) D4

Table 5. Tensile properties of AB CuCrZr specimens

Property	A1	B2	C3	D4
Yield strength (MPa)	140–160	150–170	145–165	160–180
UTS (MPa)	685	690	700	680
Uniform elongation (%)	70–75	68–72	70–75	72–75
Total elongation (%)	102–103	99–100	101–102	99–100

The AB material combines useful strength with total elongation near 100%. This suits the thermally loaded structural parts, namely the heat exchangers and rocket-nozzle components, even without heat treatment.

3.3.4 Heat-Treated CuCrZr

Heat treatment increased the strength of every specimen while retaining the ductile failure mode.

E5 yielded at 150–180 MPa and reached a UTS of 780 MPa at 80–85% strain, fracturing near 105%. F6 demonstrated the highest strength–ductility mix of all eight specimens. The observation indicated that 790 MPa at 88–92% strain, with slow neck growth and fracture at 112–114% strain, was recorded, which is the highest elongation. G7 attained the highest strength, 820 MPa at 75–80% strain, but it fractured earlier, at 95–97% strain, so its excess strength came with a small compromise in ductility. H8 was placed between them, at 805 MPa and fractured at 103–105% strain. Fig. 13 (a)-(d) corresponds to specimens E5, F6, G7 and H8 respectively.

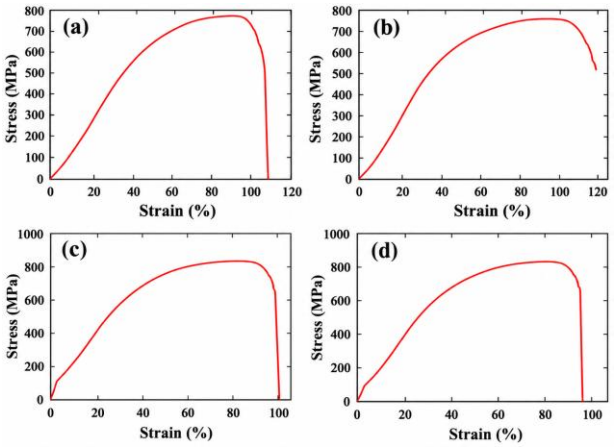

Fig. 13. Stress–strain curves of heat-treated CuCrZr specimens: (a) E5, (b) F6, (c) G7 and (d) H8

3.3.5 Effect of Heat Treatment on Tensile Performance

Comparing the two sets, heat treatment enhanced the UTS from 680–700 MPa to 780–820 MPa, a gain of about 15–18%, with no compromise on ductility. The total elongation remained at or above 95% in every heat-treated specimen, and two of the four (E5 and F6) overtook the best AB result. This strengthening is consistent with precipitation hardening, in which Cr- and Zr-rich precipitates form in the copper matrix during the thermal cycle. This blocks dislocation glide, thereby raising the stress needed for plastic flow. The one specimen that deviates from the trend is G7, which gained the most strength but compromised on some elongation, which strongly emphasizes that at very high precipitate density, the strength gains at the cost of ductility. Even so, heat-treated CuCrZr retains a strength–ductility mix that is uncommon for a precipitation-strengthened copper alloy and suits demanding aerospace, fusion-energy, and thermal-management uses. The measured hardness rise (118 to 152 HV) and this UTS rise are consistent, and both are read as the result of precipitation hardening rather than any softening of the alloy.

3.3.6 µCT of Internal Defects

The µCT cross-sections of both conditions (Fig. 14) are mostly an even grey field, as expected for a dense, well-consolidated build. Only a few isolated dark spots appear in each, grouped toward the centre and upper part of the AB scan and toward the upper-right of the heat-treated one. These mark small low-density regions, most likely shielding gas or gas trapped in the original powder. Neither scan shows the elongated, irregular dark regions along melt-pool boundaries that would signal lack-of-fusion, and neither shows cracking or interconnected porosity. Slight brightness near the edges is a reconstruction and beam-hardening artefact. Both scans indicate relative density above 99%; the defect features are summarised in Table 6.

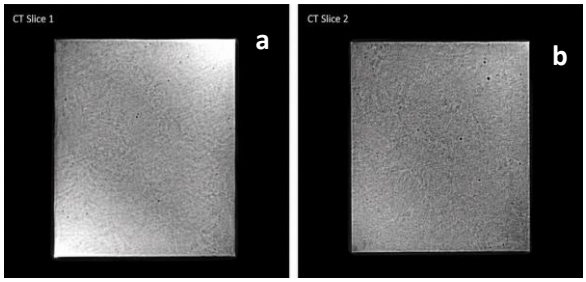

Fig. 14. µCT scans of CuCrZr: (a) AB and (b) heat-treated

Table 6. Defect features seen by µCT

Feature	As-Built	Heat-treated
Gas porosity	Isolated spherical spots, low volume fraction	Isolated spherical pores, mildly grouped in one region
Lack-of-fusion defects	Not observed	Not observed
Microcracks	Not observed	Not observed
Interconnected porosity	Not observed	Not observed
Defect distribution	Random, sparse	Sparse, mildly localised
Relative density (qualitative)	>99%	>99%

Because heat treatment mainly drives precipitation and relaxes residual stress rather than closing pores, closing the remaining porosity would need a further step such as hot isostatic pressing.

The pores in the heat-treated scan are best read as inherited from the AB state, not created by the thermal cycle. The absence of any new cracking after treatment also shows that the schedule used here did not set up damaging thermal stresses.

3.3.7 Pore Size Distribution

Fig. 15 shows the pore equivalent-diameter histograms and Table 7 lists the values. The distributions in both cases are single-peaked and right-skewed. This observation of small pores with a thin tail of larger ones is the pattern of gas porosity rather than lack-of-fusion. In the AB specimen, diameters cluster between 0.07 and 0.15 mm, with the most common band at 0.08–0.10 mm; only a few exceed 0.30 mm, and the largest was about 0.50 mm. In the heat-treated specimen, the main band sits a little higher, 0.14–0.22 mm, peaking near 140 counts in the 0.15–0.18 mm bin, with pores above 0.30 mm again rare and the largest between 0.35 and 0.39 mm.

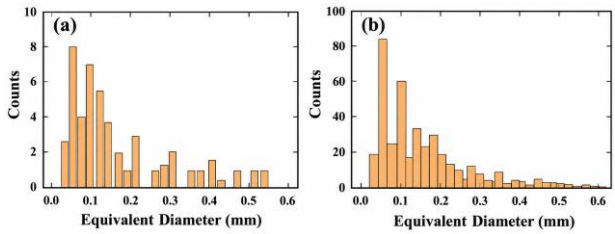

Fig. 15. Pore equivalent-diameter histograms from µCT: (a) AB and (b) heat-treated CuCrZr

Table 7. Pore-size distribution parameters from µCT

Parameter	As-Built	Heat-treated
Equivalent-diameter range	~0.06–0.50 mm	0.14–0.39 mm
Dominant pore-size range	0.07–0.15 mm	0.14–0.22 mm
Peak-frequency band	0.08–0.10 mm	0.15–0.18 mm
Distribution shape	Right-skewed	Right-skewed
Predominant defect type	Gas porosity	Gas porosity
Large pores (>0.30 mm)	Low frequency	Very low frequency
Lack-of-fusion defects	Not evident	Not evident

The two scans came from different samples and imaging sessions, so the small shift between the dominant bands most likely reflects normal specimen-to-specimen variation within the build rather than coarsening caused by the heat treatment. Both show no lack-of-fusion defects and a pore size well below 0.3 mm.

3.3.8 Linking Defects to Mechanical Behaviour

Small, isolated, near-spherical pores act only as mild stress raisers, unlike the elongated, irregular lack-of-fusion defects that are far more harmful to fatigue and tensile ductility. Since neither scan shows lack-of-fusion or interconnected porosity, the tensile results above are consistent with the µCT picture. The high density and sparse pores support the good elongation seen in both conditions, while the extra strength after heat treatment comes from precipitation hardening rather than any change in the pore population. Taken together, the results show that the LPBF settings used here were well-suited to the microstructure without harming the soundness built in during the build.

4. CONCLUSIONS

This study shows that heat treatment of LPBF CuCrZr improves both machinability and mechanical performance for high-heat-flux aerospace applications. Examinations of hardness, tensile behaviour, internal soundness and milling response together on CuCrZr present the following key points:

- Heat treatment increased the Vickers hardness from 118 ± 6 HV to 152 ± 7 HV. This clearly proves that heat treatment hardens the alloy through precipitation, but does not soften the material below the AB level. The smoother and steadier cut, respectively, is an outcome of a more uniform, stress-relieved structure, not from lower hardness.
- Heat treatment provides a more uniform, stress-relieved microstructure, leading to steadier milling and improved surface finish. The trade-off is a slightly higher CF requirement for the greater hardness. AB material cuts at slightly lower force but provides less consistent chip formation with noticeable surface tearing.
- Heat treatment increased the UTS by about 15–18%, from 680–700 MPa to 780–820 MPa due to Cr-rich and Cu–Zr precipitation, with no significant change in ductility (total elongation stayed at or above 95%).
- Specimen F6 yielded the best strength–ductility balance (790 MPa, 112–114% elongation), while G7 revealed a small strength–ductility trade-off at peak strength (820 MPa, 95–97%).
- In both cases, relative density was above 99%, with only isolated, fine, spherical gas pores.

There were no lack-of-fusion defects, microcracks or interconnected porosity, suggesting that the observed porosity is predominantly gas-related rather than associated with lack-of-fusion defects.

- Heat treatment strengthens the alloy through precipitation, while the µCT results indicate no clear change in the pore distribution; ductility is retained as the residual porosity remains fine and sparse.
- The resultant CF showed the strongest statistical association with Sa among the variables considered in the fitted model. These trends agree with published copper-machining studies, giving a practical machining window for LPBF CuCrZr parts.

Future work will extend the study to fatigue behaviour and to hot isostatic pressing as a route to close the residual gas porosity.

Conflicts of Interest

The authors declare no competing interests.

REFERENCES

[1] J. Li, Z. Kuai, Z. Li, B. Liu, Y. Chen, S. Lu, Y. Nie, Z. Yang, Effects of process parameters on the relative density and properties of CuCrZr alloy produced by selective laser melting. *Metals,* 12(5), 2022: 701. https://doi.org/10.3390/met12050701

[2] D. Cortis, E. Mancini, D. Orlandi, D. Pilone, M. Sasso, Additively manufactured CuCrZr alloy: Improvement of mechanical properties by heat treatment. *Procedia Structural Integrity,* 47, 2023: 908–914. https://doi.org/10.1016/j.prostr.2023.07.021

[3] Z. Diao, F. Yang, R. Wang, Y. Zhang, L. Chen, T. Xiong, W. Yang, M. Rong, Effect of heat treatment on the microstructure and properties of CuCrZr alloy manufactured by wire arc additive manufacturing. *Journal of Alloys and Compounds,* 967, 2023: 171786. https://doi.org/10.1016/j.jallcom.2023.171786

[4] T. Wegener, J. Koopmann, J. Richter, P. Krooß, T. Niendorf, CuCrZr processed by laser powder bed fusion — Processability and influence of heat treatment on electrical conductivity, microstructure and mechanical properties. *Fatigue & Fracture of Engineering Materials & Structures,* 44(9), 2021: 2570–2590. https://doi.org/10.1111/ffe.13527

[5] T. Baffie, G. Roux, C. Flament, M. Soulier, M. Pellat, C. Salvan, C. De Vernon, Effect of powder batches and laser power on the microstructure and properties of As-Built and heat-treated laser powder bed fusion CuCrZr samples. *World PM2022 Proceedings*, 9–13 October 2022, Lyon, France. https://doi.org/10.59499/WP225371437

[6] A.M. Khorasani, I. Gibson, A. Ghasemi, A. Ghaderi, Modelling of laser powder bed fusion process and analysing the effective parameters on surface characteristics of Ti-6Al-4V. *International Journal of Mechanical Sciences,* 168, 2020: 105299. https://doi.org/10.1016/j.ijmecsci.2019.105299

[7] D. Guillen, S. Wahlquist, A. Ali, Critical review of LPBF metal print defects detection: Roles of selective sensing technology. *Applied Sciences,* 14(15), 2024: 6718. https://doi.org/10.3390/app14156718

[8] F. Canillas, E. Leon-Gutierrez, M. Roldan, R. Hernandez, E. Urionabarrenetxea, E. Cardozo, L. Portoles, J.R. Blasco, N. Ordas, On the feasibility to obtain CuCrZr alloys with outstanding thermal and mechanical properties by additive manufacturing. *Journal of Nuclear Materials,* 601, 2024: 155304. https://doi.org/10.1016/j.jnucmat.2024.155304

[9] K. Jahns, R. Bappert, P. Böhlke, U. Krupp, Additive manufacturing of CuCr1Zr by development of a gas atomization and laser powder bed fusion routine. *The International Journal of Advanced Manufacturing Technology,* 107(5), 2020: 2151–2161. https://doi.org/10.1007/s00170-020-04941-7

[10] H. von Lintel, E. Evsiutkina, C. Haase, U. Krupp, K. Jahns, Copper alloys for additive manufacturing: Laser powder bed fusion of CuCr1Zr by using a green QCW laser. *European Journal of Materials*, 3(1), 2023: 2115945. https://doi.org/10.1080/26889277.2022.2115945

[11] P. Guan, X. Chen, P. Liu, F. Sun, C. Zhu, H. Zhou, S. Fu, Z. Wu, Y. Zhu, Effect of selective laser melting process parameters and aging heat treatment on properties of CuCrZr alloy. *Materials Research Express*, 6(11), 2019: 1165c1. https://doi.org/10.1088/2053-1591/ab4e2f

[12] J. Skiba, M. Kulczyk, S. Przybysz-Gloc, M. Skorupska, J. Smalc-Koziorowska, M. Kobus, K. Nowak, Thermo-mechanical treatment for

reducing the wear rate of CuCrZr tool electrodes during electro-discharge machining. *Materials*, 16(20), 2023: 6787. https://doi.org/10.3390/ma16206787

[13] X. Chen, P. Dong, Y. Zeng, H. Yao, J. Chen, Effect of heat treatment on the microstructure and properties of CuCrZr prepared by laser powder bed fusion. *Materials Characterization*, 214, 2024: 114103. https://doi.org/10.1016/j.matchar.2024.114103

[14] A.M. Khorasani, M.R.S. Yazdi, M.S. Safizadeh, Analysis of machining parameters effects on surface roughness: A review. *International Journal of Computational Materials Science and Surface Engineering,* 5(1), 2012: 68–84. https://doi.org/10.1504/IJCMSSE.2012.049055

[15] N. Yusup, A.M. Zain, S.Z.M. Hashim, Evolutionary techniques in optimizing machining parameters: Review and recent applications (2007–2011). *Expert Systems with Applications*, 39(10), 2012: 9909–9927. https://doi.org/10.1016/j.eswa.2012.02.109

[16] H.A. Kishawy, A. Hosseini, Environmentally conscious machining. In: *Machining Difficult-to-Cut Materials. Materials Forming, Machining and Tribology.* Springer, Cham, 2019: 205–238. https://doi.org/10.1007/978-3-319-95966-5_7

[17] H. Xie, X. Tang, F. Sun, R. Zhao, G. Li, C. Zhang, G. Huang, S. Fu, B. Peng, L. Dong, H. Chu, H. Zhou, X. Chen, P. Liu, Tensile and thermal properties, and microstructural evolution of additive-manufactured CuCrZr alloy at elevated temperature. *Journal of Materials Research and Technology,* 39, 2025: 5468–5479. https://doi.org/10.1016/j.jmrt.2025.10.172

[18] S.R. Mundla, S. Arungalai Vendan, C.P. Paul, A.K. Shettigar, C. Jambagi, Experimental investigations on the milling characteristics of Cu alloys and additively manufactured CuCrZr. *Materials Physics and Mechanics*, 53(4), 2025: 1–21. https://doi.org/10.18149/MPM.5342025_1

[19] W.M. Li, Experimental study on cutting speed and surface roughness of pure copper in WEDM. *Journal of Physics: Conference Series,* 1605, 2020: 012054. https://doi.org/10.1088/1742-6596/1605/1/012054

[20] P. Niu, Q. Cheng, W. Chang, X. Song, Y. Li, Sensitivity analysis of machining accuracy reliability considering partial correlation of geometric errors for horizontal machining center. *Proceedings of the Institution of Mechanical Engineers, Part B: Journal of Engineering Manufacture*, 235(3), 2021: 455–465. https://doi.org/10.1177/0954405420958843

[21] G.C. Ganesha, S. Arungalai Vendan, M. Chaturvedi, S.T. Chandra, Parametric analysis using Pearson heat map on ultrasonic welding of PMMA polymer deployed for structural applications. *2025 3rd International Conference on Intelligent Cyber Physical Systems and Internet of Things (ICoICI)*, 17–19 September 2025, Coimbatore, India, pp.628–632. https://doi.org/10.1109/icoici65217.2025.11253698

[22] S. Radder, M. Chaturvedi, S.A. Vendan, Comprehensive weldability analysis and morphological-thermal insights into ultrasonic welding of ABS for electronics applications. *Applied Engineering Letters*, 10(3), 2025: 125–135. https://doi.org/10.46793/aeletters.2025.10.3.1

[23] R. Zhang, J. Fang, Y. Guo, H. Li, L. Shi, P. Liu, Effect of direct aging heat treatment on microstructures and properties of CuCrZr alloy manufactured by laser powder bed fusion. *Journal of Materials Research and Technology,* 36, 2025: 8591–8601. https://doi.org/10.1016/j.jmrt.2025.05.089

© 2026 by the authors. This work is licensed under a Creative Commons Attribution-Non Commercial 4.0 International License (CC BY-NC 4.0).